CrossMark

ORIGINAL PAPER

Magnetically Recyclable Spinel Mn$_x$Ni$_{1-x}$Fe$_2$O$_4$ ($x = 0.0$–0.5) Nano-photocatalysts: Structural, Morphological and Opto-magnetic Properties

C. Barathiraja[1,2] · A. Manikandan[3] · A. M. Uduman Mohideen[1] ·
S. Jayasree[1,4] · S. Arul Antony[5]

Abstract Manganese doped nickel ferrite (Mn$_x$Ni$_{1-x}$Fe$_2$O$_4$: $x = 0.0$–0.5) spinel nanoparticles (NPs) were successfully prepared by a facile microwave combustion method (MCM) using urea as the fuel. The prepared samples were characterized by different techniques. Powder X-ray diffraction (XRD) analysis was confirmed the formation of a single-phase NiFe$_2$O$_4$ spinel structure. The average crystallite sizes of the samples were in the range of 11.49 to 17.24 nm, which was confirmed by Sherrer's formula. The morphology of the samples showed a nanoparticle-like structure with smaller agglomeration, which was confirmed by high-resolution scanning electron microscopy (HR-SEM). The particle size diameter ranges from 15 to 20 nm, which was confirmed by high-resolution transmission electron microscopy (HR-TEM). Energy dispersive X-ray (EDX) analysis confirmed the elemental composition, which was also evidence for the formation of single pure phase. Selected area electron diffraction (SAED) analysis showed well crystalline nature. UV-visible diffuse reflectance spectra (DRS) and photoluminescence (PL) spectrum analysis was used to calculate the optical band gap, and the values are slightly increased (2.02 to 2.42 eV) with increasing the Mn-dopant, due to the decreasing of particle size, which may be due to the quantum confinement effect. Magnetic properties of the samples were analyzed by vibrating sample magnetometer (VSM) technique, which showed the magnetization (M_s) value of the samples are increased with increasing Mn content and reach a maximum value of 67.82 emu/g for Mn$_{0.5}$Ni$_{0.5}$Fe$_2$O$_4$ sample. Photocatalytic activity of the samples was measured and showed the photocatalytic degradation (PCD) of methylene blue dye with good results. The catalyst was magnetically recycled and reused five consecutive cycles and showed good reproducibility without change of catalytic activity.

✉ A. Manikandan
mkavath15@gmail.com;
manikandana.che@bharathuniv.ac.in

A. M. Uduman Mohideen
amuduman14@gmail.com

1 Postgraduate and Research Department of Chemistry, Khadir Mohideen College Adirampattinam, Thanjavur 614701, Tamil Nadu, India

2 Department of Chemistry, Mannai Rajagopalaswami Government Arts College, Mannargudi 614001 Tamil Nadu, India

3 Department of Chemistry, Bharath Institute of Higher Education and Research, Bharath University, Chennai 600073, Tamil Nadu, India

4 Department of Chemistry, Kunthavai Naacchiyaar Government Arts College for Women (Autonomous), Thanjavur 613007, Tamil Nadu, India

5 Postgraduate and Research Department of Chemistry, Presidency College (Autonomous), Chennai 600005, Tamil Nadu, India

1 Introduction

Spinel type transition metal oxide magnetic nanoparticles (NPs) are considered as potential materials than that of their same bulk materials, due to their superior structutral, morphological, optical, electrical, magnetic, and catalytic properties [1–6]. Spinel ferrite (with general formula MFe$_2$O$_4$:

M = Co, Mn, Ni, etc.) NPs have much better surface area-to-volume ratio than their conservative forms, which can direct to greater chemical reactivity and alter their strength. Also, the nanoscale and quantum effects of the NPs can become much more important in determining their properties and characteristics, leading to novel optical, electrical, magnetic, and catalytic behaviors [7, 10]. Magnetic properties of the samples are depended on the nature, composition, and concentrations of the cations [9–12].

Among the various spinel ferrites, nickel ferrite (NiFe$_2$O$_4$) NPs have been used as a potential catalyst in opto-magnetic and electronic devices and photo-catalysts. Various strategies have been used for the preparation of spinel ferrites with different nanostructures such as sol-gel, thermal combustion, polyol, co-precipitation, mechanical alloying, ball milling, and hydrothermal methods [11–15]. However, the above mentioned methods meet some disadvantages such as complicated apparatus, energy overriding, and higher dispensation temperature and also need rather long reaction time to complete the crystallization of final products.

Nowadays, combustion methods have attracted considerable interest in fabricating the spinel type mixed metal oxides. Also, this method has lot of advantages such as inexpensive precursors, short preparation time and highly crystalline nature of the final products [16–18]. In this method, metal nitrates act as oxidizing agent and organic fuels such as glycine, urea, citric acid, sucrose, and hydrazine and alanine acting as reducing agent and play a vital role in determining the size, morphology and phase formation of the final products [19–25].

Organic compounds (e.g. glycine, urea, citric acid, alanine and carbohydrazide) have been mixed directly with metal nitrates to enhance the efficiency of combustion synthesis. The metal nitrates act both as oxidants and as cation sources, while the organic compound functions as the fuels [26–28]. Microwave irradiation is becoming an increasingly popular method for the synthesis of spinel materials. It offers a clean, cheap, and convenient method of heating which often results in higher yields and shorter reaction time than other methods. However, this method is fundamentally different from conventional processing. Microwave radiation is absorbed and converted to thermal energy. Heat is generated from inside the material, in contrast to conventional heating methods where heat is transferred from the outside. This internal rapid heating allows a dramatic reduction of processing time and consumed energy [29–31]. Overall the reactant precursors are fully converted into final products within a few minutes of time and no loss of elements was observed.

In the recent years, spinel type magnetic nanostructures have been widely used as an eminent material in the field of environmental applications, because of their excellent photocatalytic activity, non-toxicity, chemical stability, commercial availability and reusability. Hankare et al. [32] reported spinel ZnFe$_2$O$_4$ nanocatalyst for photocatalytic degradation (PCD) of methyl red and thymol blue. Chung et al. [33] reported the PCD of methylene blue using TiO$_2$-NiFe$_2$O$_4$ and SiO$_2$-NiFe$_2$O$_4$ prepared by spray pyrolysis method. Xiong et al. [34] reported CdS-MFe$_2$O$_4$ nanocomposites for the PCD of rhodamine B and 4-CP in aqueous solution under visible-light irradiation. Fu et al. [35] reported ZnFe$_2$O$_4$-graphene photocatalyst prepared by hydrothermal method for the PCD of methylene blue.

However, there is no literature available for the PCD of methylene blue dye using Mn-doped NiFe$_2$O$_4$ NPs prepared by microwave combustion method. When metal was doped into the spinel NiFe$_2$O$_4$, it improved their opto-magnetic and photocatalytic activity, due to their considerable morphology, smaller particle size with higher surface area. Therefore, it is highly interesting and desirable to study the spinel Mn$_x$Ni$_{1-x}$Fe$_2$O$_4$ NPs as photocatalysts for degradation of azo dyes.

2 Materials and Methods

### 2.1 Preparation of Spinel Mn$_x$Ni$_{1-x}$Fe$_2$O$_4$ (0.0 ≤ x ≤ 0.5) Nanoparticles

All chemicals such as nitrates of manganese, nickel, iron, and urea as the raw materials were used for this method. Stoichiometric amounts of corresponding metal nitrates and urea were dissolved in deionized water and stirred until a clear transparent solution was obtained. The transparent solution was placed in a microwave oven (2.45 GH and 850 W) for 10 min. Initially, the solution was subjected to boiling and underwent evaporation followed by the decomposition with the evolution of gases. When the solution reached the point of spontaneous combustion, it vaporized and instantly became solid powders. After the completion of combustion reaction, the solid powder was obtained and then it was washed well with ethanol and dried at 70 °C for 1 h, and the powders (Mn$_x$Ni$_{1-x}$Fe$_2$O$_4$ with x = 0.0, 0.1, 0.2, 0.3, 0.4, and 0.5) were labeled as NiFe$_2$O$_4$, Mn$_{0.1}$Ni$_{0.9}$Fe$_2$O$_4$, Mn$_{0.2}$Ni$_{0.8}$Fe$_2$O$_4$, Mn$_{0.3}$Ni$_{0.7}$Fe$_2$O$_4$, Mn$_{0.4}$Ni$_{0.6}$Fe$_2$O$_4$ and Mn$_{0.5}$Ni$_{0.5}$Fe$_2$O$_4$, respectively and were used for further characterizations.

2.2 Characterization Techniques

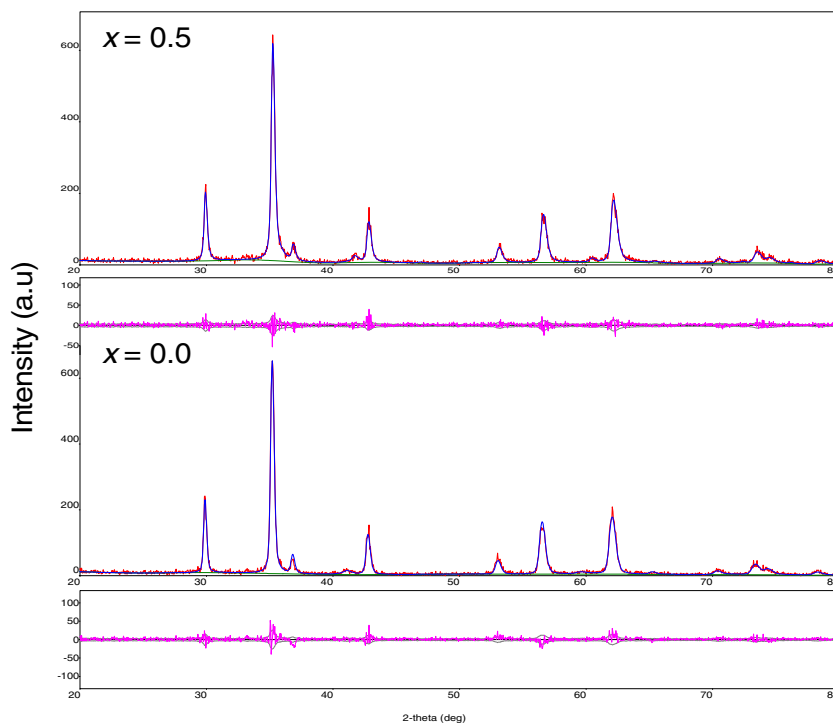The structural and phase property of Mn$_x$Ni$_{1-x}$Fe$_2$O$_4$ (x = 0.0, 0.1, 0.2, 0.3, 0.4 and 0.5) spinel nanopowders was performed using a Philips X'pert X-ray diffractometer (XRD) with CuKα radiation at λ = 1.540 Å. Structural
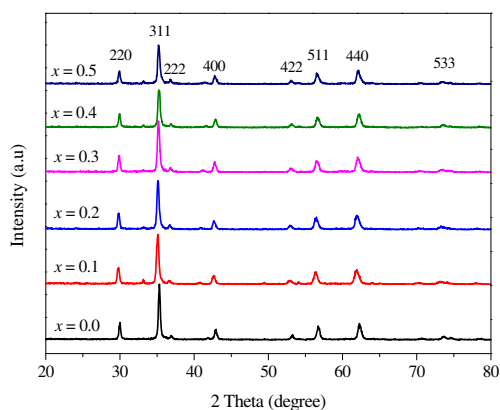
Fig. 1 Powder XRD patterns of spinel $Mn_xNi_{1-x}Fe_2O_4$ ($x = 0.0, 0.1, 0.2, 0.3, 0.4,$ and 0.5) NPs

refinements using the Rietveld refinement XRD method were carried out using PDXL program; both refined lattice parameters and crystallite size of the obtained ferrites were reported. Morphological studies and energy dispersive X-ray analysis (EDX) have been performed with a Jeol JSM6360 high-resolution scanning electron microscope (HR-SEM). The transmission electron micrographs were carried out by Philips-TEM (CM20). The surface area was derived from the N_2 adsorption-desorption isotherms using liquid nitrogen at 77 K using an automatic adsorption instrument (Quantachrome Corp. Nova-1000 gas sorption analyzer). The UV-visible diffuse reflectance spectrum (DRS) was recorded using a Cary100 UV-visible spectrophotometer to estimate their energy band gap. The

photoluminescence (PL) properties were recorded using a Varian Cary Eclipse Fluorescence Spectrophotometer. Magnetic measurements were carried out at room temperature using a PMC MicroMag 3900 model vibrating sample magnetometer (VSM) equipped with 1-T magnet.

2.3 Photocatalytic-Degradation Procedures

All photochemical reactions under identical conditions were carried out in a self-designed photocatalytic reactor. This model consists of eight medium pressure mercury vapor lamps (8 W) set in parallel and emitting 365 nm wavelength. It has a reaction chamber with specially designed reflectors made of highly polished aluminum and builtin cooling fan at the bottom and black cover to prevent UV leakage. It is provided with the magnetic stirrer at the center. Open borosilicate glass tube of 40 cm height and 12.6 mm diameter was used as a reaction vessel. The irradiation was carried out using only six parallel medium pressure mercury lamps. The solution was aerated continuously by a pump to provide oxygen and for the complete mixing of solution.

3 Results and Discussion

3.1 Powder XRD Analysis

The structural phase, crystalline nature, crystallite size, and purity of the spinel nanoparticles were confirmed by

Fig. 2 Rietveld refinement XRD method of spinel $Mn_xNi_{1-x}Fe_2O_4$ ($x = 0.0$ and 0.5) NPs

Table 1 Lattice parameter, crystallite size (Scherer formula, Rietveld analysis), and band gap of spinel $Mn_xNi_{1-x}Fe_2O_4$ ($x = 0.0, 0.1, 0.2, 0.3, 0.4,$ and 0.5) NPs

Sample	Lattice parameter (Å)	Crystallite size, L (nm)		Band gap (eV)
	Rietvela analysis	Scherrer formula	Rietveld analysis	
$NiFe_2O_4$	8.373	17.24	19	2.02
$Mn_{0.1}Ni_{0.9}Fe_2O_4$	8.381	16.52	17	2.11
$Mn_{0.2}Ni_{0.8}Fe_2O_4$	8.389	15.47	16	2.17
$Mn_{0.3}Ni_{0.7}Fe_2O_4$	8.396	14.13	15	2.25
$Mn_{0.4}Ni_{0.6}Fe_2O_4$	8.413	13.75	14	2.33
$Mn_{0.5}Ni_{0.5}Fe_2O_4$	8.422	11.49	12	2.42

analyzing the powder X-ray diffraction (XRD) patterns. Figure 1 shows the powder XRD patterns of spinel $Mn_xNi_{1-x}Fe_2O_4$ ($x = 0.0, 0.1, 0.2, 0.3, 0.4,$ and 0.5) nanoparticles. The main diffraction peaks (2θ) appear at about 30.71, 35.67, 36.95, 43.35, 53.72, 56.18, 63.45, and 74.43°, which are attributed to the (220), (311), (222), (400), (422), (511), (440), and (533) planes, respectively, and show the characteristics of a single-phase cubic spinel structure of $NiFe_2O_4$ with *Fd3m* space group (JCPDS Card No. 19-629), and all diffraction peaks could index a typical spinel-structured $NiFe_2O_4$. Powder XRD results indicates pure spinel phase, which was developed during the microwave combustion method. Moreover, a small peak is observed at $2\theta = 33.12°$, which is due to the presence of smaller amount of α-Fe_2O_3 phase. It is well known that, during the combustion process, oxidation and formation of spinel ferrites is very common. However, the formation of α-Fe_2O_3 phase was mainly due to the partial oxidation of spinel ferrites [36–38].

In order to further analyze the structural change, the measured XRD patterns were simulated based on the Rietveld refinement method (Fig. 2). From the Rietveld refinement XRD analysis, lattice parameter and crystallite size values were observed and tabulated in Table 1. It was found that the lattice parameter values are increased from 8.373 Å ($x = 0.0$) to 8.422 Å ($x = 0.5$) and is due to the substitution of smaller ionic radius of Ni^{2+} cations (0.78 Å) by the larger ionic radius of Mn^{2+} cations (0.92 Å) [39]; which is in good agreement with the Vegard's law [40]. However, the crystallite size of the samples is decreased from 19 nm ($x = 0.0$) to 12 nm ($x = 0.5$). The results revealed that it increases the concentration of Mn^{2+} ($x = 0.0$ to 0.5) and it controls and retards the growth of the crystallite size, thus confirming the smaller dimension [41–43]. Figure 3 shows the values of lattice parameter and crystallite size of the samples. However, the observed crystallite sizes of the samples are in good agreement with the values obtained from Scherrer formula.

The average crystallite size of samples was calculated using the Scherrer formula given in (1).

$$L = \frac{0.89\lambda}{\beta\cos\theta} \qquad (1)$$

where L is the average crystallite size, λ the X-ray wavelength, θ the Bragg diffraction angle, and β the peak width at half width maximum. The calculated average crystallite size is tabulated in Table 1, which indicates that the values are decreased from 17.24 nm ($x = 0.0$) to 11.49 nm ($x = 0.5$) with well crystalline nature.

The lattice parameter values were calculated using the formula given in (2):

$$\sin^2\theta = \frac{\lambda^2}{4}\left[\frac{4}{3}\left(\frac{h^2 + hk + k^2}{a^2}\right) + \frac{l^2}{c^2}\right] \qquad (2)$$

where θ is the diffraction angle, λ is the incident wavelength ($\lambda = 1.540$ Å), h, k, and l are Miller's indices. The results show that the values are increased from 3.369 Å ($x = 0.$) to 3.419 Å ($x = 0.5$) increasing the concentration of Mn^{2+} cations. The observed lattice parameter values from Rietveld refinement method are in good agreement with the calculated values. This is attributed to the different radius of Mn^{2+} (0.92 Å) and Ni^{2+} (0.78 Å). Sertkol et al. [44] synthesized spinel $Zn_xNi_{1-x}Fe_2O_4$ nanoparticles by microwave combustion method, and the lattice parameter is increased with increasing the concentration of Zn^{2+}, due to the replacement of smaller ionic radius of Ni^{2+} by larger ionic radius of Zn^{2+}. Sayed reported that $Zn_xNi_{1-x}Fe_2O_4$ spinel samples have linear increase in the lattice constant from 8.362 to 8.442 Å in between $x = 0.1$ and 0.9 [45]. In
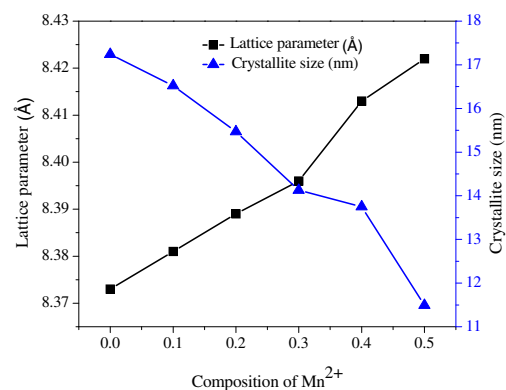
Fig. 3 Evolution of the lattice parameter and crystallite size of spinel $Mn_xNi_{1-x}Fe_2O_4$ ($x = 0.0, 0.1, 0.2, 0.3, 0.4,$ and 0.5) NPs
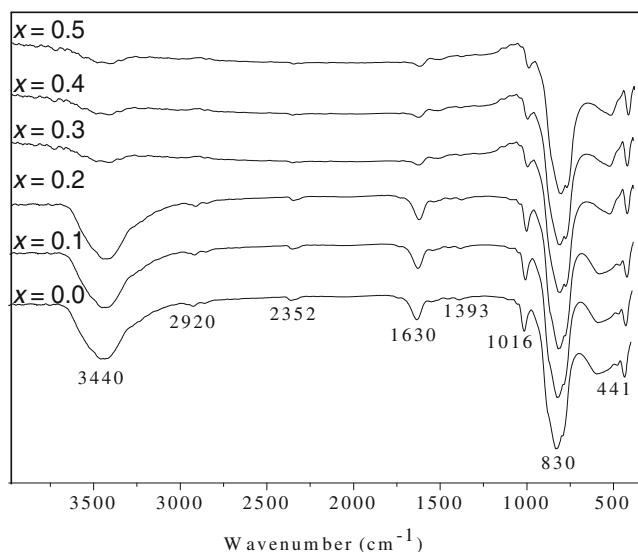
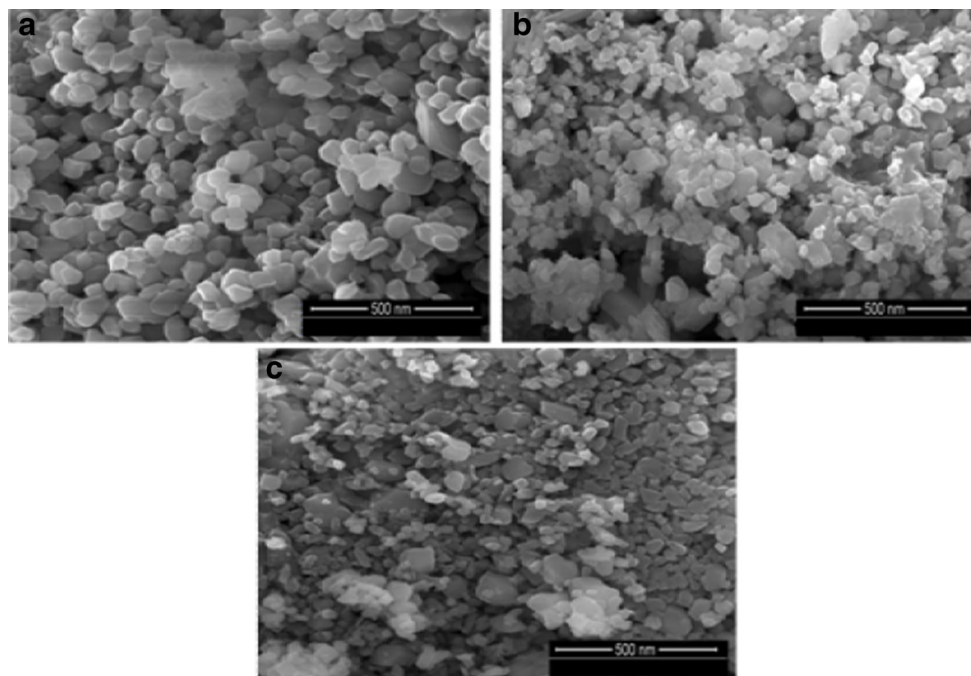**Fig. 4** FT-IR analysis of spinel $Mn_xNi_{1-x}Fe_2O_4$ (x = 0.0, 0.1, 0.2, 0.3, 0.4, and 0.5) NPs

agreement with this study, the linear increase in lattice constant from 8.373 to 8.422 Å by increasing Mn substitution was also observed [46, 47] (Fig. 3).

3.2 FT-IR Analysis

Figure 4 shows the FT-IR analysis of spinel $Mn_xNi_{1-x}Fe_2O_4$ (x = 0.0, 0.1, 0.2, 0.3, 0.4, and 0.5) NPs. Two main broad metal-oxygen bands are seen in the FT-IR spectra of all spinels and ferrites in particular. The

highest one usually observed in the range 600–550 cm^{-1} corresponds to intrinsic stretching vibrations of the metal at the A-site, $M_{tetra} \leftrightarrow O$, whereas the lowest band, typically observed in the range 450–385 cm^1, is assigned to B-site metal stretching, $M_{octa} \leftrightarrow O$ [48, 49]. However, no clear peak due to metal ions at the B- site has been observed which is predictable to occur below 400 cm^1. This may be due to the broadening of this peak attributed to very tiny particles of spinel ferrites [50]. In the FT-IR spectrum of the products, we observed a band at 600 cm^1 and assigned it as $M_{tetra} \leftrightarrow O$, due to the limitation of our FT-IR instrument bands below 400 cm^1 were not detected clearly. The bands observed at $\sim$ 3450 and $\sim$ 1630 cm^1 prove the presence of adsorbed water on the surface of the ferrite nanoparticles.

3.3 HR-SEM Analysis

Figure 5a–c shows the HR-SEM images of $NiFe_2O_4$, $Mn_{0.3}Ni_{0.7}Fe_2O_4$ and $Mn_{0.5}Ni_{0.5}Fe_2O_4$ samples, respectively. HR-SEM images reveal that the sample consists of regularshaped spherical NPs with the presence of soft agglomeration. A close view of particles also reveals that smaller crystallites have sizes less than 50 nm. In addition these smaller particles are so closely arranged together, a clear boundary between neighboring particles can still be observed.

3.4 HR-TEM Analysis

Figure 6a, b shows the HR-TEM image of undoped $NiFe_2O_4$ and $Mn_{0.5}Ni_{0.5}Fe_2O_4$ samples, respectively,

Fig. 5 HR-SEM images of spinel **a** $NiFe_2O_4$, **b** $Mn_{0.3}Ni_{0.7}Fe_2O_4$, and **c** $Mn_{0.5}Ni_{0.5}Fe_2O_4$ NPs

Fig. 6 HR-TEM images of **a**
NiFe$_2$O$_4$ and **b**
Mn$_{0.5}$Ni$_{0.5}$Fe$_2$O$_4$ NPs, and
insets shows the corresponding
SAED patterns
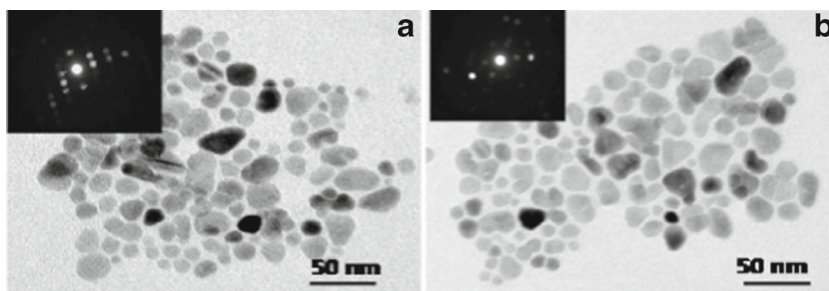
which consists of sphere-like NPs with diameter ranging
from 15 to 20 nm. Crystallite sizes obtained from XRD are
smaller than the sizes calculated from HR-TEM. In summary the particle and crystallite size estimates obtained
from different analytical methods are reasonable for the
method of synthesized NPs. Figure 6a, b (insets) shows the
SAED patterns of undoped NiFe$_2$O$_4$ and Mn$_{0.5}$Ni$_{0.5}$Fe$_2$O$_4$
samples, respectively, which implies single crystalline in
nature of the products.

3.5 EDX Analysis

Figure 7a, b shows the EDX of undoped NiFe$_2$O$_4$ and
Mn$_{0.5}$Ni$_{0.5}$Fe$_2$O$_4$ NPs and shows the peaks of Fe, Ni, and O
elements, and there is no other peak, which is confirmed that
the as-prepared samples are pure and there is no other impurity. In the EDX pattern, the presence of Fe, Ni/Mn, and O
elements in proper proportions suggested that the expected
stoichiometry was maintained in the prepared samples. The
EDX results suggested that the precursors have fully undergone the chemical reaction to form the expected single
phase NiFe$_2$O$_4$ NPs. A small gold (Au) peak appeared at

2.1 KeV for all the samples, and Au has been used as a
sputter coating for the better visibility of the surface morphology, while preparing the sample for HR-SEM analysis
[36–38].

3.6 UV-Vis DRS Study

The UV-Vis DRS has advantages over UV-Vis absorption
spectroscopy to analyze the optical properties of powdered
nanostructures, due to less scattering effects than absorption [51]. The single limitation of DRS is that the particle
size must be smaller than the wavelength of incident light.
One can use the DRS data to calculate the direct band gap
energy (E_g), as given in the Kubelka-Munk theory [52].
The Kubelka-Munk function $F(R)$ was used to calculate the
band gap (E_g) of the samples. Thus, the vertical axis is converted into quantity $F(R)$ which is equal to the absorption
co-efficient. Thus, the α in the Tauc equation is substituted
with $F(R)$ and hence the relation becomes

$$(F(R)) = \alpha = \frac{(1-R)^2}{2R} \tag{3}$$
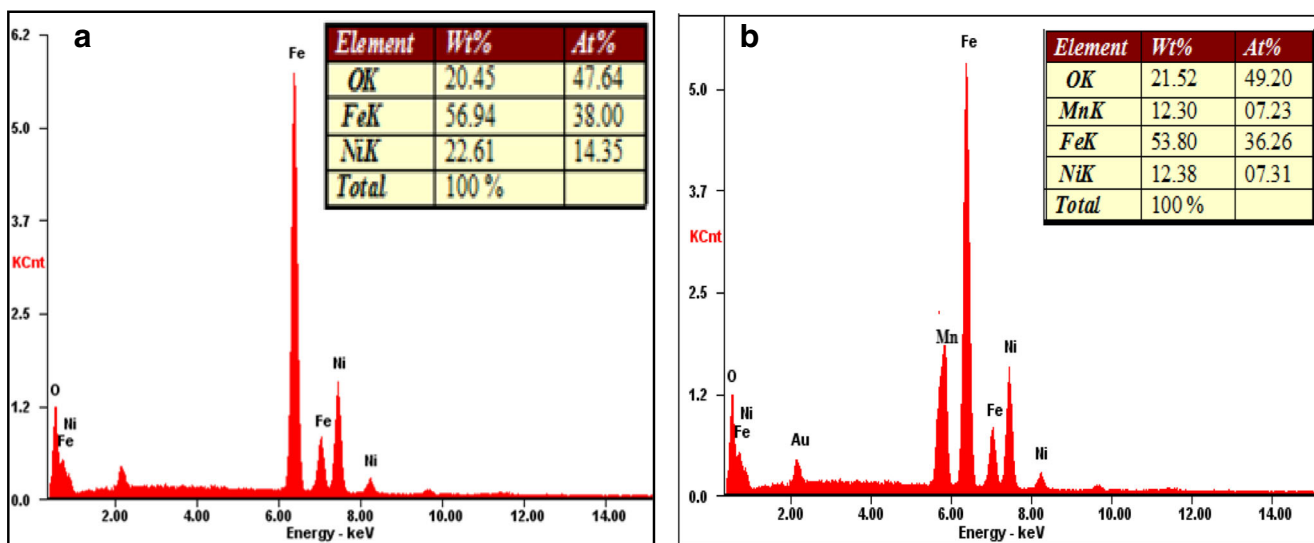
Fig. 7 EDX spectra of spinel **a** NiFe$_2$O$_4$ and **b** Mn$_{0.5}$Ni$_{0.5}$Fe$_2$O$_4$ NPs

Fig. 8 UV-Vis DRS of spinel **a** $Mn_xNi_{1-x}Fe_2O_4$ ($x = 0.0, 0.1, 0.2, 0.3, 0.4,$ and 0.5) NPs and **b** and the variation of band gap of the NPs
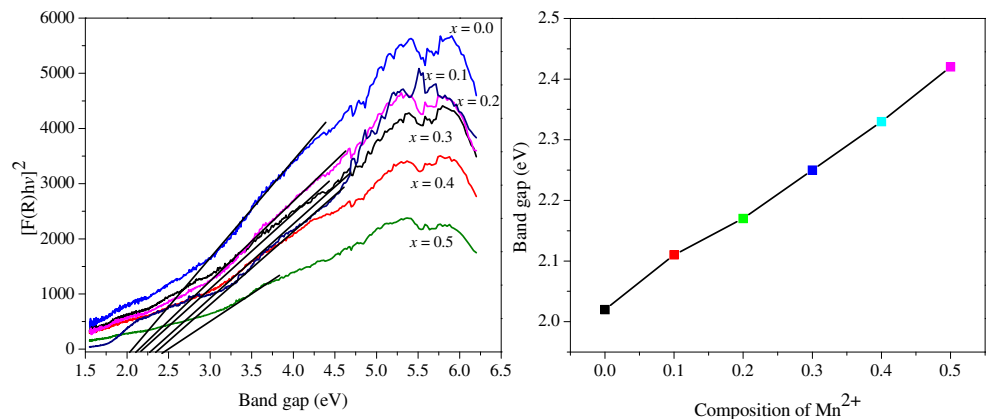
where $F(R)$ is Kubelka-Munk function, α the absorption coefficient, and R the reflectance. Thus the Tauc relation becomes

$$F(R)h\upsilon = A(h\upsilon - E_g)^n \qquad (4)$$

where A is the proportionality constant and $n = 1/2$ and 2 for direct and indirect transitions, respectively, thus giving direct and indirect band gaps. Extrapolation of linear regions of these plots to $(F(R)h\upsilon)^2 = 0$ gives the direct band gap values. In the graph, a straight line is fitted for the straight region. The extrapolation of this straight line to energy axis gives the value of the direct E_g

The E_g values for all composition of spinel $Mn_xNi_{1-x}Fe_2O_4$ is shown in Table 1 (Fig. 8a, b). The E_g values of $Mn_xNi_{1-x}Fe_2O_4$ ($x = 0.0$ to 0.5) NPs are 2.02, 2.11, 2.17, 2.25, 2.33, and 2.42 eV. The E_g of undoped $NiFe_2O_4$ NPs is 2.02 eV, and there is blue shift ($E_g = 2.11$ to 2.42 eV) for all Mn-doped samples ($x = 0.1$ to 0.5), indicating that these NPs may have visible-light photoactivity. This is mainly attributed to the reduction in crystallite size of $NiFe_2O_4$ NPs as Mn content increase. The shift in E_g of the $Mn_xNi_{1-x}Fe_2O_4$ NPs with the decreasing crystallite size is the result of quantum confinement effects arising from the small size regime.

3.7 Photoluminescence Study

Figure 9 shows the photoluminescence (PL) spectra of spinel $Mn_xNi_{1-x}Fe_2O_4$($x = 0.0$ to 0.5) NPs. All compositions were excited by using the excitation wavelength at 385 nm which shows the characteristic NBE emissions at around 403 and 425 nm. For the applications of electronic devices, such as high-efficiency UV light-emitting devices, it is significant to the visible emission with enhanced UV emission. The observed broad band NBE emissions at 403 nm (3.07 eV) and 425 nm (2.91 eV) can be assigned to interstitial metal defects and oxygen vacancies [53–55].

The blue emission bands at around 453 nm (2.73 eV) and 470 nm (2.63 eV) can be assigned to intrinsic defects,

particularly interstitial defects. In the visible region, green emission band observed at 504 nm (2.46 eV) may be attributed to the impurity levels correspond to the oxygen vacancy in $NiFe_2O_4$. The composition with $x = 0.5$ shows highest PL intensity; this can be attributed to the appearance of new electronic levels between conduction band (CB) and valence band (VB) and might be due to the increase of intrinsic defects in the compositions.

3.8 VSM Analysis

Figure 10 shows the magnetization measurements for $Mn_xNi_{1-x}Fe_2O_4$ NPs with different Mn contents ($x = 0.0, 0.1, 0.2, 0.3, 0.4$ and 0.5) in which M_s values are obtained as 34.92, 39.59, 48.79, 56.02, 58.56 and 67.82 emu/g, respectively (Table 2). The coercivity, H_c, values were found to be decreased from $x = 0.0$ (131.61 Oe) to $x = 0.5$ (60.18 Oe). The M_s of these samples is smaller than that observed for the bulk (65–115 emu/g) and the H_c of the samples with Mn contents of 0.0 to 0.5 are much greater than the bulk values [56, 57]. These differences can be attributed to spin-disorder on the surface, spin-canting, spin-glass-like behavior in surface layers of NPs, due to local chemical disorder, and
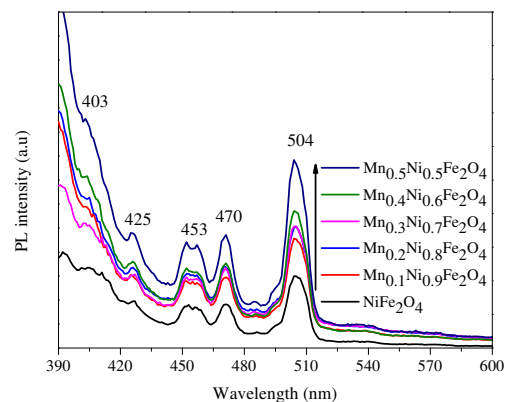
Fig. 9 PL spectra of spinel $Mn_xNi_{1-x}Fe_2O_4$ ($x = 0.0, 0.1, 0.2, 0.3, 0.4,$ and 0.5) NPs
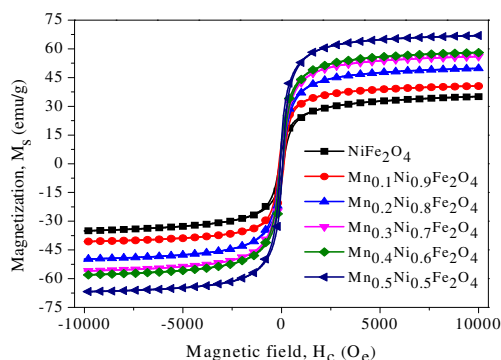
Fig. 10 $M - H$ loops of spinel $Mn_xNi_{1-x}Fe_2O_4$ ($x = 0.0$, 0.1, 0.2, 0.3, 0.4, and 0.5) NPs

broken exchange interactions [58, 59]. They can also be attributed to the enhancement of the surface barrier potential, due to the distortion of crystal lattice caused by the atoms deviating from normal positions in the surface layer. All of these factors may lead to a smaller M_s and H_c than bulk [45]. The increase of M_s with increasing the Mn concentration have been explained on the basis of higher and lower magnetic moments of Mn and Ni respectively. Mn^{2+} (high-magnetic) ions prefer A and B lattice and transfer some Fe^{3+} ions with large magnetic moment to B site, thus resulting in an increase in M_s. Therefore, different magnetic behaviors of ferrite nanocrystals can be attributed to dominant ferromagnetic coupling of Fe ions at A–B sites and surface spin canting. The decrease in H_c with the increase in Mn content can also be attributed to the reduction in the number of spins occupying the A sub-lattices, causing the net magnetization to increase with Mn concentration.

The spinel $NiFe_2O_4$ forms as inverse spinel ferrite with Ni^{2+} ions occupying B site and Fe^{3+} equally distributed at A and B sites. The magnetic Mn^{2+} (5 μB) ions have leads to the transfer of Fe^{3+} ions from A to B site. The incorporation of high magnetic moment of Mn^{2+} (5 μB) ions into the B-sublattices instead of low magnetic moment of Ni^{2+} (2 μB) ions leads to a greater increase in the magnetic moment per formula unit of the B site when preference to both A and B sites of the spinel lattice. The replacement of Ni^{2+} ions

Table 2 Variation of H_c, M_r, and M_s of spinel $Mn_xNi_{1-x}Fe_2O_4$ ($x = 0.0$, 0.1, 0.2, 0.3, 0.4, and 0.5) NPs

| Samples	H_c (Oe)	M_r (emu/g)	M_s (emu/g)
$NiFe_2O_4$	131.81	6.69	34.92
$Mn_{0.1}Ni_{0.9}Fe_2O_4$	101.62	11.41	39.59
$Mn_{0.2}Ni_{0.8}Fe_2O_4$	85.57	9.31	48.78
$Mn_{0.3}Ni_{0.7}Fe_2O_4$	75.29	10.05	56.02
$Mn_{0.4}Ni_{0.6}Fe_2O_4$	74.52	10.47	58.56
$Mn_{0.5}Ni_{0.5}Fe_2O_4$	60.18	12.58	67.82

compared with the A site. Also, the occupancy of Mn^{2+} ion in A site allows the Fe^{3+} ions to migrate from A to B site and willingly increases the overall magnetic moment. However, the very low values of H_c and M_r, indicate that they are also soft magnets.

3.9 Photocatalytic Activity

It has been usually accepted that the crystallinity, particle size, concentrations of doping metal ions, and morphologies of the nanomaterials are significant factors that influence its photocatalytic performance. Jia et al. [60] reported that the photocatalytic activity of spinel $ZnFe_2O_4$ nanostructures obviously relies on surface properties and surface defects. Therefore, it is important to prepare $NiFe_2O_4$ ($0.0 \leq x \leq 0.5$) NPs and understand the chemistry occurring at Mn doping and tune the photocatalytic degradation of methylene blue dye. Thus, we made an attempt to reveal the relationship between optical and photocatalytic properties of $NiFe_2O_4$ and Mn-doped $NiFe_2O_4$ NPs and a series of experiments were carried out under the light of wavelength 365 nm.

3.9.1 Effects of Mn Doping on the Photocatalytic Activity of $NiFe_2O_4$ NPs

The influence of Mn doping on $NiFe_2O_4$ NPs on the PCD efficiency was evaluated and is shown in Fig. 11. The PCD efficiency of undoped $NiFe_2O_4$ is very low, and it is increased with increase in the concentration of Mn doping and showed a maximum activity at $x = 0.5$ ($Mn_{0.5}Ni_{0.5}Fe_2O_4$). This may be due to the smaller particle size distribution and higher surface area of $Mn_{0.5}Ni_{0.5}Fe_2O_4$ NPs. However, our present study confirms the photocatalytic activity of single phase spinel $NiFe_2O_4$ is enhanced when an addition of Mn content.
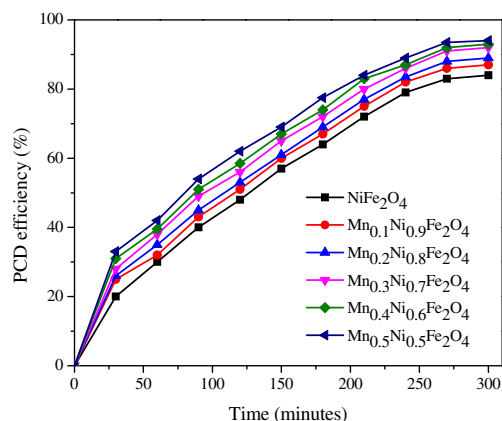
Fig. 11 Effect of Mn doping on the PCD efficiency of $NiFe_2O_4$ photocatalyst

3.9.2 Effect of Surface Area on the Photocatalytic Activity of $NiFe_2O_4$ NPs

In general, a high specific surface area has a favorable effect on the activity for photo-catalysts. Surface area of the nano-materials is very important for the photocatalytic activity. In addition, when the size of particles decreases, the amount of the dispersion of particles per volume in the solution will increase, which results in the enhancement of the photon absorbance. Surface areas of $NiFe_2O_4$, $Mn_{0.1}Ni_{0.9}Fe_2O_4$, $Mn_{0.2}Ni_{0.8}Fe_2O_4$, $Mn_{0.3}Ni_{0.7}Fe_2O_4$, $Mn_{0.4}Ni_{0.6}Fe_2O_4$, and $Mn_{0.5}Ni_{0.5}Fe_2O_4$ NPs are 21.17, 23.34, 25.43, 27.49, 29.82 and 31.65 m^2/g, respectively. The surface area is increased with increasing the concentration of Mn content ($x = 0.5$), and the sample $Mn_{0.5}Ni_{0.5}Fe_2O_4$ was found to have a higher surface area (31.65 m^2/g) than other samples. Besides, as the particle size decreases, the number of active surface sites increased. Therefore, it is believed that the high surface area of $Mn_{0.5}Ni_{0.5}Fe_2O_4$ NPs could enhance the photocatalytic properties than that of other samples (Fig. 11). It is found that the high specific surface area of $Mn_{0.5}Ni_{0.5}Fe_2O_4$ NPs was beneficial to photocatalytic activity via attractive the adsorption of azo dyes, which is the determining step in the heterogeneous photocatalytic reaction. Usually, photocatalyst with a high specific surface area would offer more surface active sites and photocatalytic reaction centers, resulting in the enhancement of photocatalytic performance. Thus, the higher surface area of $Mn_{0.5}Ni_{0.5}Fe_2O_4$ NPs may lead to higher photocatalytic activity, as compared to other samples [61].

4 Conclusions

Spinel $Mn_xNi_{1-x}Fe_2O_4$ ($x = 0.0-0.5$) NPs were successfully prepared by microwave combustion method using urea as a fuel. Powder XRD, Rietveld refinement XRD, FT-IR, SAED, and EDX analysis were confirmed the formation of spinel phase $NiFe_2O_4$ powders without any other secondary phase formation with well-crystallized nanoparticles. The average crystallite size was calculated from the XRD peaks confirmed the range of 11.49–17.24 nm in size. HR-SEM and HR-TEM analysis showed the particle-like morphology of the samples with agglomeration. UV-visible DRS and PL spectrum analysis showed the optical band gap of the samples and the values are slightly increased with decreasing the crystallite size, which may be due to the quantum confinement effect. VSM technique shows the saturation magnetization (M_s) value of the samples increased with increasing Mn content to reach a maximum value of 67.82 emu/g for $Mn_{0.5}Ni_{0.5}Fe_2O_4$ and it was confirmed that ferromagnetic behavior. PCD of azo dyes was carried out and observed good results than the reported results.

References

1. Manikandan, A., Sridhar, R., Arul Antony, S., Ramakrishna, S.: J. Mol. Struct. **1076**, 188 (2014)
2. Amir, Md., Geleri, M., Guner, S., Baykal, A., Sozeri, H.: J. Inorg. Organomet. Polym. **25**, 1111 (2015)
3. Manikandan, A., Saravanan, A., Arul Antony, S., Bououdina, M.: J. Nanosci. Nanotech. **15**, 4358 (2015)
4. Manikandan, A., Durka, M., Arul Antony, S.: J. Supercond. Nov. Magn. **28**, 209 (2015)
5. Amir, Md., Baykal, A., Guner, S., Sertkol, M., Sozeri, H., Toprak, M.: J. Inorg. Organomet. Polym. **25**, 747 (2015)
6. Manikandan, A., Durka, M., Arul Antony, S.: J. Supercond. Nov. Magn. **27**, 2841 (2014)
7. Manikandan, A., Arul Antony, S.: Supercond. Nov. Magn. **27**, 2725 (2014)
8. Manikandan, A., Arul Antony, S., Sridhar, R., Bououdina, M.: J. Nanosci. Nanotech. **15**, 4948 (2015)
9. Manikandan, A., Durka, M., Arul Antony, S.: J. Inorg. Organomet. Polym. **25**, 804 (2015)
10. Manikandan, A., Hema, E., Durka, M., Seevakan, K., Alagesan, T., Arul Antony, S.: J. Supercond. Nov. Magn. **28**, 1783 (2015)
11. Manikandan, A., Durka, M., Arul Antony, S.: J. Supercond. Nov. Magn. **28**, 2047 (2015)
12. Amir, Md., Sertkol, M., Baykal, A., Sozeri, H.: J. Supercond. Nov. Magn. **28**, 2447 (2015)
13. Baykal, A., Deligöz, H., Sozeri, H., Durmus, Z., Toprak, M.S.: J. Supercond. Nov. Magn. **25**, 1879 (2012)
14. Shafiu, S., Sozeri, H., Baykal, A.: J. Supercond. Nov. Magn. **27**, 1593 (2014)
15. Baykal, A., Durmus, Z., Toprak, M.S., Sozeri, H.: J. Supercond. Nov. Magn. **25**, 2003 (2012)
16. Manikandan, A., John Kennedy, L., Bououdina, M., Judith Vijaya, J.: Ceram. Int. **39**, 5909 (2013)
17. Manikandan, A., John Kennedy, L., Bououdina, M., Judith Vijaya, J.: J. Magn. Magn. Mater. **349**, 249 (2014)
18. Amir, Md., Baykal, A., Sertkol, M., Sözeri, H.: J. Inorg. Organomet. Polym. **25**, 619 (2015)
19. Amir, Md., Unal, B., Shirsath, S.E., Geleri, M., Sertkol, M., Baykal, A.: Superlatt. Microstruct. **85**, 747 (2015)
20. Manikandan, A., John Kennedy, L., Bououdina, M., Judith Vijaya, J.: J. Mol. Struct. **1035**, 332 (2013)
21. Guner, S., Amir, Md., Geleri, M., Sertkol, M., Baykal, A.: Ceram. Int. **41**, 10915 (2015)
22. Baykal, A., Amir, Md., Güner, S., Sözeri, H.: J. Magn. Magn. Mater. **395**, 199 (2015)
23. Manikandan, A., John Kennedy, L., Judith Vijaya, J.: J. Nanosci. Nanotech. **13**, 2986 (2013)
24. Jayasree, S., Manikandan, A., Uduman Mohideen, A.M., Barathiraja, C., Arul Antony, S.: Adv. Sci. Eng. Med. **7**, 672 (2015)
25. Ozkaya, T., Baykal, A., Kavas, H., Koseoglu, Y., Toprak, M.S.: Physica B **403**, 3760 (2008)
26. Kasapoglu, N., Baykal, A., Koseoglu, Y., Toprak, M.S.: Scripta Mater. **57**, 441 (2007)
27. Sayed, A.M.E.: Ceram. Int. **28**, 363 (2002)
28. Baykal, A., Kasapoglu, N., Koseoglu, Y., Basaran, A.C., Kavas, H., Toprak, M.S.: Cent. Eur. J. Chem. **6**, 125 (2008)
29. Hwang, C.C., Wu, T.Y., Wan, J., Tsai, J.S.: Mater. Sci. Eng. B **111**, 49 (2004)
30. Rao, K.J., Vaidhyanathan, B., Ganguli, M., Ramakrishnan, P.A.: Chem. Mater. **11**, 882 (1999)
31. Ma, Y., Vileno, E., Suib, S.L., Dutta, P.K.: Chem. Mater. **9**, 2023 (1997)
32. Hankare, P.P., Patil, R.P., Jadhav, A.V., Garadkar, K.M., Sasikala, R.: App. Catal. B: Env. **107**, 333 (2011)

33. Chung, Y.S., Park, S.B., Kang, D.W.: Mater. Chem. Phys. **86**, 375 (2004)
34. Xiong, P., Zhu, J., Wang, X.: Ind. Eng. Chem. Res. **52**, 17126 (2013)
35. Fu, Y., Wang, X.: Ind. Eng. Chem. Res. **50**, 7210 (2011)
36. Manikandan, A., Durka, M., Arul Antony, S.: Adv. Sci. Eng. Med. **7**, 33 (2015)
37. Manikandan, A., Durka, M., Seevakan, K., Arul Antony, S.: J. Supercond. Nov. Magn. **28**, 1405 (2015)
38. Valan, M.F., Manikandan, A., Arul Antony, S.: J. Nanosci. Nanotech. **15**, 4543 (2015)
39. Kavas, H., Baykal, A., Toprak, M.S., Koseoglu, Y., Sertkol, M., Aktas, B.: J. Alloys Compd. **479**, 49 (2009)
40. Gao, J., Cui, Y., Yang, Z.: Mater. Sci. Eng. B **110**, 111 (2004)
41. Manikandan, A., Durka, M., Autha Selvi, M., Arul Antony, S.: J. Nanosci. Nanotech. **16**, 448 (2016)
42. Hema, E., Manikandan, A., Karthika, P., Arul Antony, S., Venkatraman, B.R.: J .Supercond. Nov. Magn. **28**, 2539 (2015)
43. Manikandan, A., Durka, M., Autha Selvi, M., Arul Antony, S.: J. Nanosci. Nanotech. **16**, 357 (2016)
44. Sertkol, M., Koseoglu, Y., Baykal, A., Kavas, H., Bozkurt, A., Toprak, M.S.: J. Alloys Compd. **486**, 325 (2009)
45. Sayed, A.M.E.: Ceram. Int. **28**, 363 (2002)
46. Smit, J., Wijn, H.P.J.: Ferrites, vol. 44, Philips Techno Library, Eindwen, Netherlands 58 (1959)
47. Joshi, H.H., Kulkarni, R.G.: J. Mater. Sci. **21**, 2138 (1986)
48. Narayanasamy, A., Sivakumar, N.: Bull. Mater. Sci. **31**, 373 (2005)
49. Ajmal, M., Maqsood, A.: Mater. Lett. **62**, 2077 (2008)
50. Azadmanjiri, J.: Mater. Chem. Phys. **109**, 109 (2008)
51. Girgis, E., Wahsh, M.M.S., Othman, A.G.M., Bandhu, L., Rao, K.V.: Nano Res. Lett. **6**, 460 (2011)
52. Kubelka, P., Munk, F.: Z Tech. Phys. **12**, 593 (1931)
53. Manikandan, A., Judith Vijaya, J., Sundararajan, M., Meganathan, C., John Kennedy, L., Bououdina, M.: Superlatt. Microstruct. **64**, 118 (2013)
54. Manikandan, A., John Kennedy, L., Arul Mary, J., Dinesh, A., Judith Vijaya, J.: J. Ind. Eng. Chem. **20**, 2077 (2014)
55. Mary Jacintha, A., Manikandan, A., Chinnaraj, K., Arul Antony, S., Neeraja, P.: J. Nanosci. Nanotech. **15**, 9732 (2015)
56. Swaminathan, R., McHenry, M.E., Poddar, P., Srikanth, H.: J. Appl. Phys. **97**, G104 (2005)
57. Zhang, H.E., Zhang, B.F., Wang, G.F., Dong, X.H., Gao, Y.: J. Magn. Magn. Mater. **312**, 126 (2007)
58. Brabers, V.A.M.: Phys. Stat. Sol. **33**, 563 (1969)
59. Koseoğlu, Y.: Ceram. Int. **41**, 6417 (2015)
60. Jia, Z., Ren, D., Liang, Y., Zhu, R.: Mater. Lett. **65**, 3116 (2011)
61. Xiong, P., Zhu, J., Wang, X.: Ind. Eng. Chem. Res. **52**, 17126 (2013)